Improvement of magnetic field detectivity in electrical 1/*f* noise-dominated tunnel magnetoresistive sensors by AC magnetic field modulation technique

Tomoya Nakatani,* Hirofumi Suto, Prabhanjan D. Kulkarni, Hitoshi Iwasaki, and Yuya Sakuraba

Research Center for Magnetic and Spintronic Materials, National Institute for Materials Science, 1-2-1 Sengen, Tsukuba, Ibaraki, 305-0047, Japan

* Corresponding author: nakatani.tomoya@nims.go.jp

Abstract

Suppression of 1/*f* noise in tunnel magnetoresistance (TMR) sensors is a central issue in the realization of magnetic field sensors with ultrafine magnetic field detectivity. Although AC modulation with an external magnetic field has been proposed as a method to shift the operating frequency of a sensor to a high frequency and substantially suppress 1/*f* noise, its effects on the two types of 1/*f* noise, that is, magnetic and electrical 1/*f* noise, are not well understood. In this study, we investigated the noise characteristics and signal detection performance of TMR sensors with an even-function resistance-magnetic field curve operated by the AC modulation method. For one TMR device in which the magnetic 1/*f* noise was dominant, AC modulation degraded the magnetic field detectivity owing to the additional noise induced by the AC modulation field. However, in another TMR device, in which the electrical 1/*f* noise was artificially enhanced by introducing lattice defects in the MgO tunnel barrier, AC modulation effectively suppressed the 1/*f* noise and improved the magnetic field detectivity by one order.

This demonstrates that the AC modulation method using an external magnetic field is effective for magnetic field sensors in which electrical 1/*f* noise is dominant.

I. Introduction

Magnetoresistive (MR) sensors, such as giant magnetoresistance (GMR) and tunnel magnetoresistance (TMR) sensors, offer various magnetic field-sensing applications. One of the most challenging applications is the detection of ultra-small magnetic fields such as biomagnetic fields for magnetocardiogram and magnetoencephalogram, which are sub-pT-level AC magnetic fields at low frequencies (typically 0.1-100 Hz).[1–5] For these applications, obtaining MR sensors with small magnetic field detectivities (*D*) is critical, where *D* is defined by $D = \sqrt{S_V}/\left(\frac{dV}{dH}\right)$, where $\sqrt{S_V}$ is the noise voltage density, and $\frac{dV}{dH}$ is the output voltage sensitivity of the sensor. *D* indicates the magnetic field-equivalent noise level of the sensor. At low frequencies, the noise of the MR sensors is dominated by 1/*f* noise, which has both electrical and magnetic origins.[6–8] The electrical 1/*f* noise originates from lattice defects, and the quality of the tunnel barrier greatly affects the electrical 1/*f* noise in TMR sensors.[9,10] On the other hand, the magnetic 1/*f* noise is attributed to the thermal fluctuations of the magnetization and the magnetic domain wall.[6,7,11,12] Reducing the 1/*f* noise in MR devices has been the central issue for magnetic sensors, and has been achieved in various ways; e.g., by selecting appropriate ferromagnetic materials,[13–15] using an MgO tunnel barrier or optimizing its fabrication process,[4,9,10,16] connecting many individual MR devices,[17–19] chopping techniques,[20,21] and AC modulation techniques.[22–25]

The typical AC modulation method using movable magnetic flux concentrators fabricated by microelectromechanical systems modulates the frequency of the signal field to

the sidebands of the carrier frequency of the AC modulation (f_{ac}), by which we can avoid the low-frequency regime where the 1/*f* noise is dominant. Therefore, we can effectively suppress the noise of the MR sensor.[22,23] However, the major challenge in applying this AC modulation method is the large output signal of the AC modulation at f_{ac}, which makes it difficult to detect the weak magnetic fields whose signals appear in the sidebands of f_{ac}. Recently, another AC modulation method using an external AC magnetic field was proposed.[26,27] This method uses GMR or TMR devices with symmetric changes in resistance (*R*) with respect to the sign of the magnetic field (*H*), that is, even-function *R*-*H* response curves. An AC modulation field with f_{ac} in the kHz range is applied along the sensing axis of the sensor. The output signal of a sensing field at a frequency of f_{sen} is modulated to $f_{ac}\pm f_{sen}$, whereas the output signal of the modulation field appears at $2f_{ac}$ due to the even-function *R*-*H* curve, thus the output signals of the sensing field and the modulation field are sufficiently separated in frequency. Therefore, this method is expected to improve (decrease) the *D* value of the MR sensors. Note that the improvement of *D* is due to the transfer of the output signal of the sensing field to a higher frequency, thus the 1/*f* noise is not intrinsically suppressed. However, from the user's point of view, the noise of the sensor appears to be effectively suppressed. Therefore, in this study, we often use the expression "suppression" for the effect of the AC modulation method on the 1/f noise.

We recently reported that magnetic 1/*f* noise is also transferred by the AC modulation field; therefore, magnetic 1/*f* noise cannot be avoided by this method.[28] This is because the virtual magnetic field that causes the thermal fluctuation of magnetization is indistinguishable from the actual magnetic field to be detected. This implies that the 1/*f* noise of electrical origin, which has no susceptibility to magnetic field, can be avoided (or effectively suppressed) by this AC modulation method; however, quantitative investigations have not been reported. Therefore, the main purpose of this study is to investigate whether the electrical 1/*f* noise at low frequencies

is avoided by the AC modulation using an external magnetic field. Using a TMR sensor device in which the electrical 1/*f* noise was artificially enhanced, we demonstrated that the electrical 1/*f* noise was avoided by the AC modulation method and that the magnetic field detectivity was improved.

II. Experimental procedures

The TMR sensor devices used in this study are composed of the *soft-pinned* free layer (FL) structure, where the FL is weakly pinned unidirectionally.[28–30] Figure 1(a) shows the structure of the TMR sensors used in this study. We sputter-deposited bottom electrode/Ta (2)/Ru (2)/IrMn (6)/CoFe (2)/AgSn spacer (2.8)/CoFe (1)/CoFeBTa (20)/Ta (0.3)/CoFeB (3)/MgO (2)/CoFeB (2.5)/Ta (0.3)/CoFeB (0.5)/CoFe (1)/Ru (0.8)/CoFe (3)/IrMn (8)/Ru (8) cap (thickness in nm). The nominal compositions of the alloy layers were $Ir_{20}Mn_{80}$, $Co_{50}Fe_{50}$, $Ag_{90}Sn_{10}$, $Co_{38}Fe_{38}B_{19}Ta_5$, and $Co_{40}Fe_{40}B_{20}$ (at. %). The CoFe/CoFeBTa/Ta/CoFeB layers below the MgO barrier act as a soft-pinned FL whose pinning strength is adjusted by the ferromagnetic orange-peel coupling through the AgSn spacer.[28] We fabricated two types of samples (devices A and B) with a difference in the magnitude of the electrical 1/*f* noise. For device B, we artificially introduced lattice defects into the MgO barrier by exposing it to Ar plasma before depositing the subsequent layers. On the other hand, device A as a control sample was fabricated without the Ar plasma exposure. The details of this process are described in the Supplementary materials.

The TMR films were patterned into 40-μm diameter devices down to the MgO tunnel barrier, whereas the FL was patterned into a 400×180 μm rectangular shape. After completion of the microfabrication process, the devices were annealed at 350 °C for 1 h under a magnetic field of 0.5 T. As shown in Fig. 1(a), the magnetization directions of the reference layer and FL

point in opposite directions in the *x* direction at zero external magnetic field, and the device has a magnetic hard axis (HA) in the *y* direction, which is the sensing axis. The *R*-*H* curves of the TMR devices were measured using the four-terminal method with a constant bias current of 0.1-1.0 mA using a source measure unit. An AC modulation field was applied along the HA using a coil fabricated on a printed circuit board, on which the substrate of the TMR device was placed. The Joule heating of the coil limited the maximum amplitude of the AC field (H_{ac}) to ~1 mT_{rms}. Noise measurements were performed using the four-terminal method in a permalloy magnetic shield box, and the TMR devices were electrically biased using a dry cell and a ballast resistor. The bias voltage (V_b) was set to V_{b0} = 40 mV at H = 0, where the sensor resistance (R) was maximized (R_{max}). Because R changes with H, V_b follows $V_b = R/R_{max} \cdot V_{b0}$. Details of the sample properties, processes, and measurements are described in our previous publication.[28]

III. Results and discussion

A. TMR properties

Figures 1(b) and (c) show the *R*-*H* curves of the TMR sensors without (device A) and with (device B) Ar plasma exposure process to the MgO barrier, respectively. When H was applied in the easy axis (EA) in the *x* direction, device A showed a TMR ratio of 218% and a resistance-area product in the parallel magnetization state (RA_P) of ~72 kΩ μm^2. The shift of the *R*-H_x curve from H = 0 corresponds to the soft-pinning strength (H_{sp}) of the FL of 0.9 mT, and the soft-pinned FL showed an EA coercivity (H_c^{EA}) of 0.9 mT. For H in the HA, the *R*-H_y curve showed an even-function curve with negligible magnetic hysteresis. Device B showed similar H_{sp} of 1.2 mT and H_c^{EA} of 0.9 mT in the EA, but with a much lower TMR ratio of 71% (RA_P ~9 kΩ μm^2). Nevertheless, device B exhibits a non-hysteretic even-function *R*-H_y curve. Because both devices showed similar H_{sp} and H_c^{EA}, the Ar plasma was considered to introduce

lattice defects in the MgO barrier. The soft-pinned FL was practically intact, which was also suggested by the additional experimental observations described in the supplementary materials.

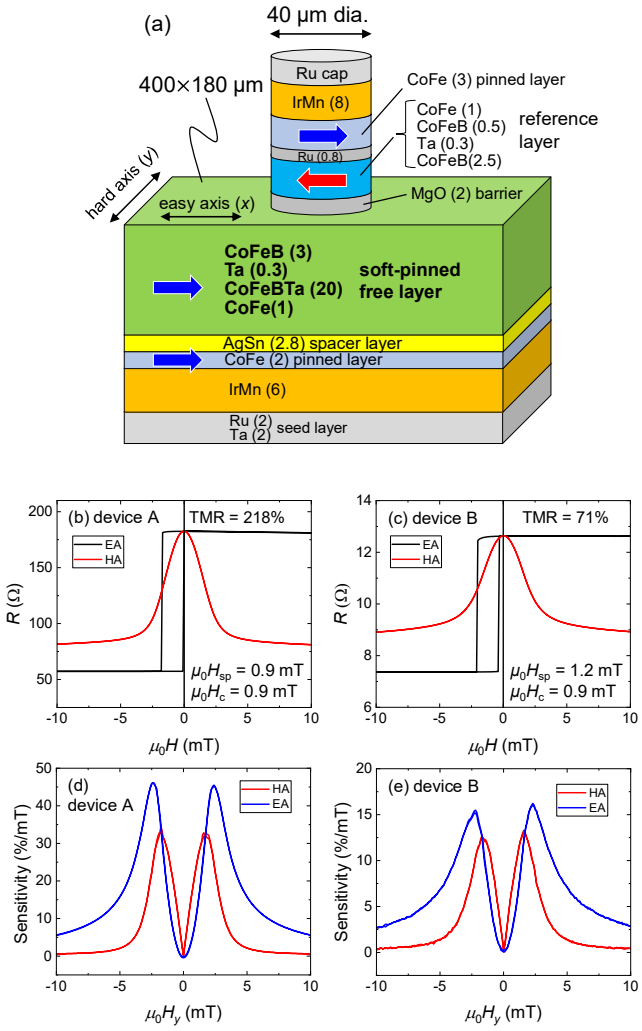

FIG. 1. (a) Schematic structure of the TMR devices with a soft-pinned FL. The bottom and top electrodes and the SiO_2 insulating layer around the pillar are not shown. The arrows drawn on the ferromagnetic layers are their magnetization directions at H = 0. (b) and (c) show R-H curves of devices A (control sample) and B (MgO barrier exposed to Ar plasma), respectively, for EA and HA. (d) and (e) show HA and EA sensitivity (S_{HA} and S_{EA}) curves of device A and B, respectively.

Figures 1(d) and (e) show the sensitivity curves of devices A and B, respectively. The HA sensitivity (S_{HA}) is the numerical derivative of the R-H_y curve normalized by R, i.e., $S_{HA} = \frac{dR}{dH_y} \cdot \frac{1}{R}$, which determines the output voltage (V_{out}) as $V_{out} = S_{HA} V_b H_{sig}$, where H_{sig} is the amplitude of an AC signal field. On the other hand, the EA sensitivity (S_{EA}), which is not a derivative of the R-H_x curve, was measured by the change in the R-H_y curve under a small bias magnetic field in the EA (x direction). S_{EA} gives the intensity of the noise caused by magnetization fluctuation, which was described in detail in our previous publication.[28] For both samples, S_{HA} and S_{EA} showed maximum value at $|\mu_0 H_y|$ = 1.5 and 2.5 mT, respectively.

B. Noise properties

We characterized the noise and signal field detection characteristics of devices A and B in two types of sensor operation modes. The first one was under a static bias field H_y, where the devices gained non-zero sensitivity (Figs. 1(d) and (e)). The other was under an AC modulation field at f_{ac} = 1−30 kHz applied to the HA; no static bias field was applied. We applied AC signal fields at 30 Hz with amplitudes of 31 nT_{rms} and 93 nT_{rms} to devices A and B, respectively. The choice of 30 Hz was arbitrary. The larger amplitude of the signal field for device B was because this device was too noisy to detect the 31 nT_{rms} field. The signal-to-noise ratio (SNR) was defined as $\mathrm{SNR} = 20\log\left(\sqrt{S_V^{sig}} / \sqrt{S_V^{noise}}\right)$, where $\sqrt{S_V^{sig}}$ and $\sqrt{S_V^{noise}}$ are the voltage densities ($\sqrt{S_V}$) of the signal and noise at 30 Hz, respectively.

(i) Device A fabricated without Ar plasma exposure to MgO barrier

Figure 2(a) shows the $\sqrt{S_V}$ spectra of device A under the bias fields in HA (H_y). Because the S_{HA} of this device was zero at H_y = 0, as shown in Fig. 1(d), the $\sqrt{S_V}$ spectrum at

H_y = 0 exhibited only noise with a 1/*f* characteristic without a signal peak at 30 Hz. When H_y was applied, the device obtained a non-zero S_{HA}, and the 31 nT_{rms} signal field was detected, as indicated by the peaks at 30 Hz. Simultaneously, the intensity of the 1/*f* noise increased with increasing H_y owing to the contribution of the magnetic 1/*f* noise. The $\sqrt{S_V}$ spectra were fitted by $\sqrt{S_V} = \left(S_V^{wh} + \alpha_H V_b^2 A^{-1} f^{\beta}\right)^{1/2}$, where S_V^{wh} is the power spectral density of the white noise, α_H is the Hooge parameter of 1/*f* noise, *A* is the area of the MTJ, and β is the exponent of *f*. As shown in Fig. 2(b), α_H increased with increasing H_y, except for the noisy spot at $\mu_0 H_y$ = 1.7 mT, which was characteristic of this particular device. The inset of Fig. 2(b) shows a linear dependence of α_H on S_{EA}, consistent with the fluctuation-dissipation relation for magnetic 1/*f* noise.[6] However, the slope of the α_H vs. S_{EA} dependence changes at S_{EA} ~ 10 %/mT, whose origin remains unclear. Figure 2(c) shows the H_y-dependencies of the signal and noise amplitudes at 30 Hz. The noise amplitude at 30 Hz was extrapolated from the values at 25-29 and 31-35 Hz, as shown in the inset of Fig. 2(a). The signal amplitude is saturated at $\mu_0 H_y$ ~1.5 mT, which is consistent with the saturation of the S_{HA} at $\mu_0 H_y$ ~1.5 mT (Fig. 1(d)). Consequently, the SNR for the 31 nT_{rms} signal field is saturated to ~17 dB at $\mu_0 H_y$ ~1.5 mT. From the relationship of SNR = 20 log (*Sig*/*D*), where *Sig* is the spectral density of the signal field (31 $nT/Hz^{0.5}$ in this case) and *D* is the detectivity, the minimum *D* of device A at 30 Hz was 4.4 $nT/Hz^{0.5}$, which is close to the value of *D* (4.0 $nT/Hz^{0.5}$ at 30 Hz) calculated from the noise amplitude and S_{HA} by the definition of $D = \sqrt{S_V}/(S_{HA} \cdot V_b)$.

This device with an area *A* of 1256 μm^2 showed a smaller *D* compared to the TMR device with a CoFeB (2)/Ta (0.21)/NiFe (4) FL with *A* = 2463 μm^2 showing *D* = 8.6 $nV/Hz^{0.5}$ (30 Hz).[31] However, TMR devices with CoFeSiB-based FLs have been reported to show superior performance of *D*. Huang *et al.*[14] reported *D* = 4.5 $nT/Hz^{0.5}$ (10 Hz) using a single TMR sensor device (*A* = 300 μm^2) with a CoFe (3)/Ru (0.2)/CoFeSiB (30) FL. Oogane *et al.*[4]

reported $D \sim 10$ pT/Hz$^{0.5}$ (30 Hz) using an array of 74 TMR devices (A of each device was 250 μm^2) with a CoFeB (3)/Ru (0.4)/CoFeSiB (140) FL. Thus, the application of the amorphous CoFeSiB soft magnetic layer may further reduce the D of our TMR sensors.

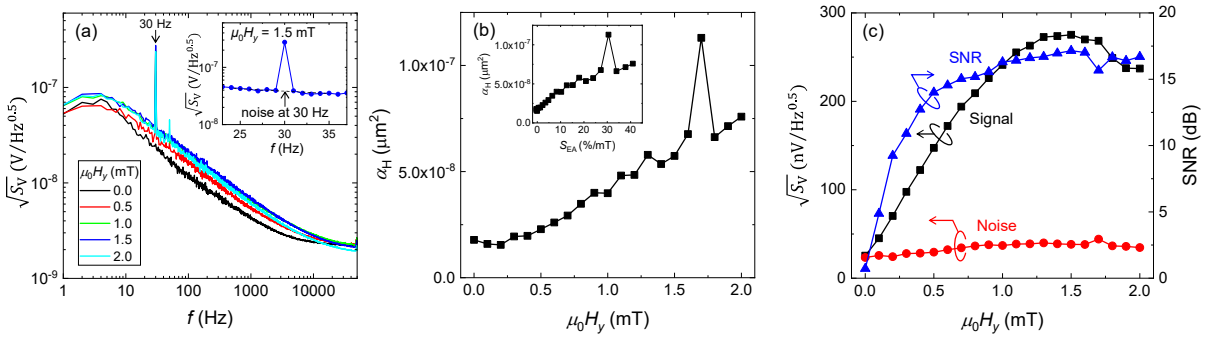

FIG. 2. (a) Voltage density spectra of device A under static bias magnetic fields in HA (H_y). The output signals of the 31 nT$_{rms}$ field are observed at 30 Hz (b) Hooge parameter (α_H) vs. H_y. The inset shows a linear relationship between α_H and S_{EA}. (c) Dependences of the signal and noise at 30 Hz and signal-to-noise ratio (SNR) on H_y.

Next, the signal detection of device A using AC modulation (f_{ac} = 1−30 kHz) was tested. The even-function R-H curves of the TMR sensors can be approximated by quadratic functions for small H_y. Therefore,

$$R = aH_y{}^2 + R_{\max}, \qquad (1)$$

where a (< 0) is a coefficient and $R_{\max}$ is the maximum resistance of the sensor at $H_y = 0$. When an AC modulation field and an AC signal field, i.e., $H_y = H_{ac} \sin \omega_{ac} t + H_{sig} \sin \omega_{sig} t$, are applied, the voltage across the sensor is expressed as:

$$V = I_b R$$

$$= I_b a \left\{ -\frac{H_{ac}{}^2}{2} \cos 2\omega_{ac} t - H_{ac} H_{sig} \left[\cos(\omega_{ac} + \omega_{sig}) t - \cos(\omega_{ac} - \omega_{sig}) t \right] - \right.$$

$$\frac{{H_{\mathrm{sig}}}^2}{2}\cos 2\omega_{\mathrm{sig}}t\Big\} + V_{\mathrm{DC}}\,, \qquad (2)$$

where I_{b} is the bias current, and $V_{\mathrm{DC}} = \frac{I_{\mathrm{b}}a}{2}\left({H_{\mathrm{ac}}}^2 + {H_{\mathrm{sig}}}^2\right) + I_{\mathrm{b}}R_{\mathrm{max}}$. The second and third terms in Eq. (2) are the signal components in the sidebands of f_{ac}, which are re-written as

$$V_{\mathrm{signal}} = -\frac{V_{\mathrm{b}}}{R}\cdot\left.\frac{dR}{dH_y}\right|_{H_y=H_{\mathrm{ac}}}\frac{1}{2H_{\mathrm{ac}}}\cdot H_{\mathrm{ac}}H_{\mathrm{sig}}\left[\cos\left(\omega_{\mathrm{ac}}+\omega_{\mathrm{sig}}\right)t - \cos\left(\omega_{\mathrm{ac}}-\omega_{\mathrm{sig}}\right)t\right]$$

$$= -\frac{V_{\mathrm{b}}}{2}\cdot S_{\mathrm{HA}}(H_{\mathrm{ac}})\cdot H_{\mathrm{sig}}\left[\cos\left(\omega_{\mathrm{ac}}+\omega_{\mathrm{sig}}\right)t - \cos\left(\omega_{\mathrm{ac}}-\omega_{\mathrm{sig}}\right)t\right], \qquad (3)$$

where we used the relations of $I_b = \frac{V_{\mathrm{b}}}{R}$, $a = \frac{dR}{dH_y}\frac{1}{2H_y}$ (from Eq. (1)), and $S_{\mathrm{HA}}(H_y) = \frac{dR}{dH_y}\frac{1}{R}$. Therefore, the output voltage of the signal field is proportional to the product of $S_{\mathrm{HA}}(H_{\mathrm{ac}})$ and H_{sig}.

Figure 3(a) shows the $\sqrt{S_{\mathrm{V}}}$ spectra for different H_{ac} values at f_{ac} = 10 kHz. The 30 Hz signal field is modulated to (f_{ac}±30) Hz. As shown in Fig. 3(b), the signal amplitude at (f_{ac}±30) Hz increased with increasing H_{ac} due to the increasing S_{HA} in the range of H_y (Fig. 1(d)). As H_{ac} increases, the noise level also increases with two types of characteristics, as reported previously.[28] One is noise with a flat spectrum, as observed at $f < f_{\mathrm{ac}}$ shown in Fig. 3(a), which is attributed to random telegraph noise (RTN) caused by the creation and annihilation of small magnetic domains under an AC modulation field. The other is observed as a skirt-like spectrum in the sideband of the f_{ac} peak (see the inset of Fig. 3(a)), which is attributed to the transfer of magnetic 1/*f* noise to f_{ac}. Due to these types of additional noises, the noise level at (f_{ac}±30) Hz showed a linear increase with increasing H_{ac}. Consequently, as shown in Fig. 3(c), the SNR was approximately constant at ~11 dB, much lower than the 17 dB measured under a bias H_y of ~1.5 mT. Therefore, *D* at 30 Hz under the AC modulation was 8.7 nT/Hz$^{0.5}$, which was higher than the *D* of 4.4 nT/Hz$^{0.5}$ under the bias H_y. Therefore, for the regular TMR devices, where the magnetic 1/*f* noise is dominant, the AC modulation by an external magnetic field degrades *D*.

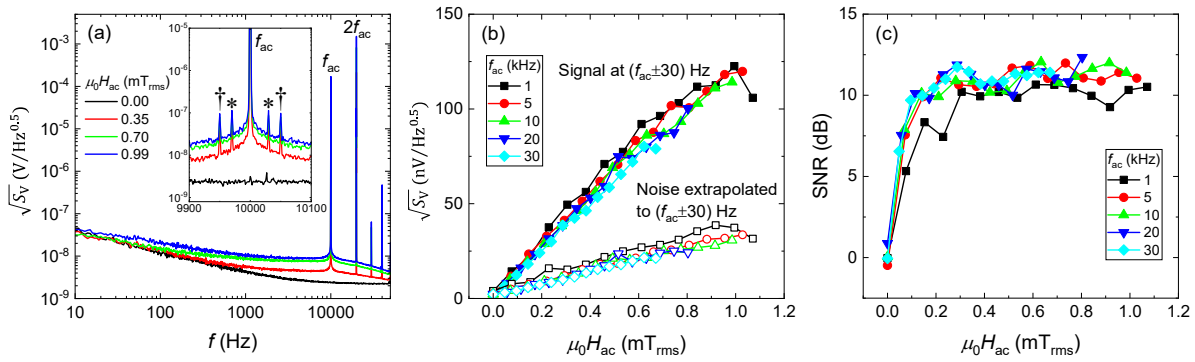

FIG. 3. (a) Voltage density spectra of device A under AC modulation fields at f_{ac} = 10 kHz. The inset shows the spectra around f_{ac}. The peaks marked with an asterisk (*) indicate the modulated signals of the 30 Hz, 31 nT$_{rms}$ field and those marked with a dagger (†) are 50 Hz noise from the power line. The H_{ac}-dependences of (b) the signal and noise at (f_{ac}±30) Hz, and (c) the SNR of the signal field.

(ii) Device B with artificially induced lattice defects in MgO barrier

We performed the same tests for device B, in which the MgO barrier was exposed to Ar plasma. Figure 4(a) shows the $\sqrt{S_V}$ spectra under static H_y, which exhibits 1/f noise up to 100 kHz. As shown in Fig. 4(b), α_H of device B was ~5×10^{-6} μm^2, two orders of magnitude larger than that of device A (Fig. 2(b)). Because the FLs of devices A and B have similar magnetic properties, that is, H_{sp} and H_c^{EA}, as shown in Figs. 1(b) and (c), respectively, the magnetic 1/f noises in these two devices are expected to be similar. Thus, the larger noise in device B is attributed to the electrical 1/f noise induced by the Ar plasma damage in the MgO barrier. This is also consistent with the observation that α_H did not increase with increasing S_{EA} (the inset of Fig. 4(b)). Although α_H decreases with increasing H_y, the origin is unclear at present. This may be related to the decrease in device resistance with increasing H_y. As shown in Fig. 4(a), the 93 nT$_{rms}$ signal field was detected only for $\mu_0 H_y \geq 0.8$ mT, indicating $D > 93$ nT/Hz$^{0.5}$

at 30 Hz for $\mu_0 H_y$ < 0.8 mT. Fig. 4(c) shows the H_y-dependence of the SNR for the 93 nT_{rms} signal field. The maximum SNR was ~6 dB at $\mu_0 H_y$ ~ 1.5 mT; therefore, the minimum D was ~50 $nT/Hz^{0.5}$ at 30 Hz, which was approximately ten times larger than that of device A. Figure 4(c) shows the values of D calculated by $D = \sqrt{S_V}/(S_{HA} \cdot V_b)$ and similar values to those calculated from the SNR of the signal field.

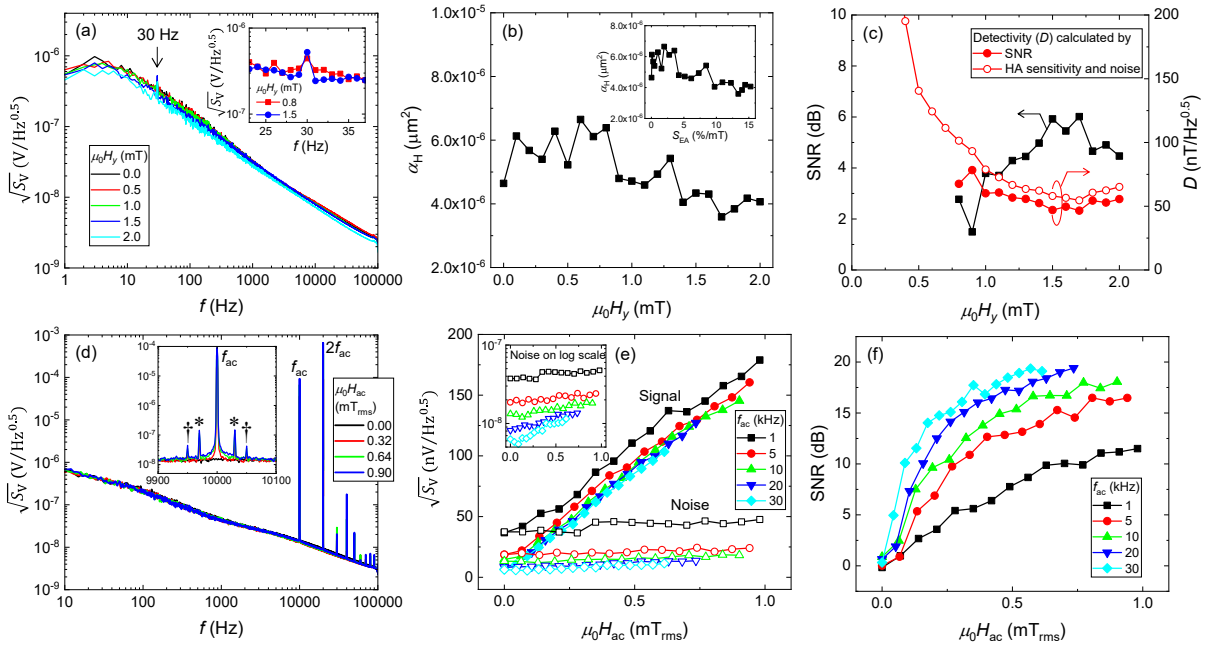

FIG. 4. (a) Voltage density spectra of device B under static bias magnetic fields (H_y), and (b) the H_y-dependence of α_H. The inset of (b) shows α_H plotted for S_{EA}. (c) The H_y-dependences of SNR for 30 Hz, 93 nT signal field, and D. (d) Voltage density spectra of device B under AC modulation field at f_{ac} = 10 kHz with various amplitudes (H_{ac}). The peaks marked with an asterisk (*) and a dagger (†) in the inset figure are the modulated signal and 50 Hz noise, respectively. The H_{ac}-dependences of (e) the signal and noise at (f_{ac}±30) Hz, and (f) the SNR of the signal field. The inset of (e) shows the noise voltage density at (f_{ac}±30) Hz on the logarithmic scale.

The results of the AC modulation experiments for device B are shown in Figs. 4(d)-(f).

Compared to device A, the overall noise characteristics of device B did not significantly change when applying the AC modulation fields. This indicates that the electrical 1/*f* noise induced by the Ar plasma damage dominates the total noise of this device and that the RTN under the AC modulation field has a comparatively small contribution. The signal peaks were observed at (f_{ac}±30) Hz, as shown by the asterisks in the inset of Fig. 4(d), demonstrating that the AC magnetic field modulation technique can effectively reduce electrical 1/*f* noise by transferring the output signal to the sidebands of f_{ac}. Figures 4(e) and (f) show the H_{ac}-dependences of the signal and noise amplitudes at (f_{ac}±30) Hz and SNR, respectively. The signal and noise amplitudes increased linearly with increasing H_{ac} because S_{HA} and S_{EA} increased approximately linearly with increasing H_y in this range, as shown in Fig. 1(e). Compared to device A (Fig. 3(b)), device B showed a smaller increase in the noise amplitude with H_{ac}. This is explained by both smaller S_{EA} of device B (Figs. 1(d) and (e)) and smaller contribution of RTN in device B. For a given value of H_{ac}, a higher f_{ac} decreases the noise amplitude at (f_{ac}±30) Hz, approximately following the $S_V \propto 1/f_{ac}$ relationship. Therefore, the SNR improved more significantly at higher f_{ac} values, as shown in Fig. 4(f). The maximum SNR for the 93 nT_{rms} signal field within these measurements was 19.3 dB for $\mu_0 H_{ac}$ = 0.7 mT_{rms}; therefore, D = 10 nT/$Hz^{0.5}$ at 30 Hz. Compared to the D value of ~ 100 nT/$Hz^{0.5}$ obtained by applying a static bias field of $\mu_0 H_y$ = 0.7 mT (Fig. 4(b)), the AC modulation method reduced D by a factor of ten. Although in these experiments the f_{ac} and H_{ac} were limited by the impedance and Joule heating of the coil to generate the AC modulation field, AC modulations with higher f_{ac} and larger H_{ac} could further improve the SNR and D.

IV. Conclusions

We have investigated the effects of AC magnetic field modulation on the electrical and

magnetic 1/*f* noise and magnetic field detection performance of TMR sensors with even-function *R*-*H* curves. In a regular TMR sensor, the low-frequency noise is dominated by the magnetic 1/*f* noise, for which no improvement in the magnetic field detectivity is obtained by the AC modulation method. This is due to the RTN and the transfer of the magnetic 1/*f* noise by the AC modulation field. However, in a TMR device in which the electrical 1/*f* noise is artificially enhanced by exposing the MgO barrier to Ar plasma, the electrical 1/*f* noise is effectively suppressed by transferring the output signal to high frequencies by the AC magnetic field modulation, which improves the magnetic field detectivity of the sensor. Since the noise in TMR devices with superparamagnetic FLs has been reported to be dominated by electrical 1/*f* noise,[32–34] the superparamagnetic granular TMR devices with even-function *R*-*H* curves[35] are worthy of further investigation in combination with the AC modulation method.

Supplementary material

Refer to the supplementary materials for the details of the Ar plasma exposure process and additional data on its effect on the TMR ratio and noise characteristics.

Acknowledgments

This work was partly supported by JSPS KAKENHI (grant number 20K04588). We thank Satoshi Shirotori, Yoshihiro Higashi, and Akira Kikitsu (Toshiba Corporation R&D Center) for fruitful discussions.

Author Declarations

The authors have no conflicts to disclose.

Data Availability Statement

The data supporting the findings of this study are available from the corresponding author upon reasonable request.

References

[1] M. Pannetier, C. Fermon, G. Le Goff, J. Simola, and E. Kerr, Science (80-.). **304**, 1648 (2004).

[2] R.C. Chaves, P.P. Freitas, B. Ocker, and W. Maass, Appl. Phys. Lett. **91**, 102504 (2007).

[3] K. Fujiwara, M. Oogane, A. Kanno, M. Imada, J. Jono, T. Terauchi, T. Okuno, Y. Aritomi, M. Morikawa, M. Tsuchida, N. Nakasato, and Y. Ando, Appl. Phys. Express **11**, 023001 (2018).

[4] M. Oogane, K. Fujiwara, A. Kanno, T. Nakano, H. Wagatsuma, T. Arimoto, S. Mizukami, S. Kumagai, H. Matsuzaki, N. Nakasato, and Y. Ando, Appl. Phys. Express **14**, 123002 (2021).

[5] A. Kanno, N. Nakasato, M. Oogane, K. Fujiwara, T. Nakano, T. Arimoto, H. Matsuzaki, and Y. Ando, Sci. Rep. **12**, 6106 (2022).

[6] H.T. Hardner, M.B. Weissman, M.B. Salamon, and S.S.P. Parkin, Phys. Rev. B **48**, 16156 (1993).

[7] N. Smith, A.M. Zeltser, D.L. Yang, and P. V. Koeppe, IEEE Trans. Magn. **33**, 3385 (1997).

[8] W.F. Egelhoff, P.W.T. Pong, J. Unguris, R.D. McMichael, E.R. Nowak, A.S. Edelstein, J.E. Burnette, and G.A. Fischer, Sensors Actuators A Phys. **155**, 217 (2009).

[9] A. Gokce, E.R. Nowak, S.H. Yang, and S.S.P. Parkin, J. Appl. Phys. **99**, 08A906 (2006).

[10] A.F. Md Nor, T. Kato, S.J. Ahn, T. Daibou, K. Ono, M. Oogane, Y. Ando, and T. Miyazaki, J. Appl. Phys. **99**, 08T306 (2006).

[11] S. Ingvarsson, G. Xiao, S.S.P. Parkin, W.J. Gallagher, G. Grinstein, and R.H. Koch, Phys. Rev. Lett. **85**, 3289 (2000).

[12] A. Ozbay, A. Gokce, T. Flanagan, R.A. Stearrett, E.R. Nowak, and C. Nordman, Appl. Phys. Lett. **94**, 202506 (2009).

[13] D. Kato, M. Oogane, K. Fujiwara, T. Nishikawa, H. Naganuma, and Y. Ando, Appl. Phys. Express **6**, 103004 (2013).

[14] L. Huang, Z.H. Yuan, B.S. Tao, C.H. Wan, P. Guo, Q.T. Zhang, L. Yin, J.F. Feng, T. Nakano, H. Naganuma, H.F. Liu, Y. Yan, and X.F. Han, J. Appl. Phys. **122**, 113903 (2017).

[15] M. Rasly, T. Nakatani, J. Li, H. Sepehri-Amin, H. Sukegawa, and Y. Sakuraba, J. Phys. D. Appl. Phys. **54**, 095002 (2021).

[16] J. Scola, H. Polovy, C. Fermon, M. Pannetier-Lecœur, G. Feng, K. Fahy, and J.M.D. Coey, Appl. Phys. Lett. **90**, 252501 (2007).

[17] R. Guerrero, M. Pannetier-Lecoeur, C. Fermon, S. Cardoso, R. Ferreira, and P.P. Freitas, J. Appl. Phys. **105**, 113922 (2009).

[18] W. Zhang, Q. Hao, and G. Xiao, Phys. Rev. B **84**, 094446 (2011).

[19] K. Fujiwara, M. Oogane, T. Nishikawa, H. Naganuma, and Y. Ando, Jpn. J. Appl. Phys. **52**, 04CM07 (2013).

[20] A. Jander, C.A. Nordman, A. V. Pohm, and J.M. Anderson, J. Appl. Phys. **93**, 8382 (2003).

[21] V.-S. Luong, C.-H. Chang, J.-T. Jeng, C.-C. Lu, J.-H. Hsu, and C.-R. Chang, IEEE Trans. Magn. **50**, 4005904 (2014).

[22] A.S. Edelstein and G.A. Fischer, J. Appl. Phys. **91**, 7795 (2002).

[23] A.S. Edelstein, G.A. Fischer, M. Pedersen, E.R. Nowak, S.F. Cheng, and C.A. Nordman, J. Appl. Phys. **99**, 08B317 (2006).

[24] J. Hu, Q. Du, J. Zhang, M. Pan, K. Sun, H. Luo, X. Zhang, and Y. Yu, AIP Adv. **12**,

025318 (2022).

[25] W. Zhao, X. Tao, C. Ye, and Y. Tao, Sensors **22**, 1021 (2022).

[26] A. Bocheux, C. Cavoit, M. Mouchel, C. Ducruet, R. Fons, P. Sabon, I.L. Prejbeanu, and C. Baraduc, 2016 IEEE Sensors Appl. Symp. 1 (2016).

[27] S. Shirotori, A. Kikitsu, Y. Higashi, Y. Kurosaki, and H. Iwasaki, IEEE Trans. Magn. **57**, 4000305 (2021).

[28] T. Nakatani, H. Suto, P.D. Kulkarni, H. Iwasaki, and Y. Sakuraba, Appl. Phys. Lett. **121**, 192406 (2022).

[29] R. Ferreira, E. Paz, P.P. Freitas, J. Wang, and S. Xue, IEEE Trans. Magn. **48**, 3719 (2012).

[30] J.Y. Chen, J.F. Feng, and J.M.D. Coey, Appl. Phys. Lett. **100**, 142407 (2012).

[31] J.P. Valadeiro, J. Amaral, D.C. Leitao, R. Ferreira, S.F. Cardoso, and P.J.P. Freitas, IEEE Trans. Magn. **51**, 4400204 (2015).

[32] P. Wisniowski, J.M. Almeida, and P.P. Freitas, IEEE Trans. Magn. **44**, 2551 (2008).

[33] K. Ishikawa, M. Oogane, K. Fujiwara, J. Jono, M. Tsuchida, and Y. Ando, Jpn. J. Appl. Phys. **55**, 123001 (2016).

[34] Y. Zhang, G. He, X. Zhang, and G. Xiao, Appl. Phys. Lett. **115**, 022402 (2019).

[35] N. Kobayashi, S. Ohnuma, S. Murakami, T. Masumoto, S. Mitani, and H. Fujimori, J. Magn. Magn. Mater. **188**, 30 (1998).

Supplementary materials

1. Ar plasma damage in MgO tunnel barrier

In the present work, we artificially induced lattice defects in the MgO tunnel barrier of the TMR device to manipulate the intensity of the electrical 1/*f* nose. This was achieved by exposing the MgO barrier (2 nm) to an Ar plasma. The Ar plasma was generated by an RF reserve-sputtering stage of our sputter deposition system. In the deposition system, there is a significant leakage of the RF power to the ground, thus the exact RF power density on the sample surface is not known. However, we have confirmed that the physical etching rate for MgO by the Ar plasma is negligibly small. From the following experimental observations, we consider that the Ar plasma exposure process creates lattice defects only in the surface of the MgO barrier and the property of the soft-pinned FL remains unchanged.

First, we compare the TMR characteristics of two devices, device B and C, which are prepared differently as shown in the flowchart of Fig. S1(a). Device B is the same as in this paper, where the MgO barrier (2 nm) was exposed to the Ar plasma for 30 s. Device C was fabricated similarly, but the Ar plasma exposure for 30 s was placed after the deposition of half of the MgO barrier, *i.e.*, 1 nm, followed by another deposition of 1 nm of MgO. Both devices were annealed at 350 °C for 1 h under a magnetic field of 0.5 T after the device fabrication. Figures S1(b) and (c) show the distributions of *RA* in the parallel magnetization state *vs*. TMR ratio of the devices fabricated on the substrates of device B and C, respectively. Device B showed large distributions of *RA* and TMR ratio among the nominally identical devices, suggesting that the degree of damage caused by the Ar plasma exposure differed from device to device. The TMR ratio of device B was at most 100%, much lower than the TMR ratio of 218% for device A fabricated without Ar plasma exposure (see Fig. 1(b)). On the other hand,

device C showed an almost constant TMR ratio of 214%. For this device, the observed *RA* distribution was as usual for our deposition system, which was due to the non-uniformity of the MgO thickness. The inset of Fig. S1(c) shows the *R*-*H* curves of a 40-μm diameter device C, showing a soft-pinning field (H_{sp}) of 1.1 mT and a coercivity (H_c) of 0.9 mT, very close to those of devices A and B (see Figs. 1(b) and (c)).

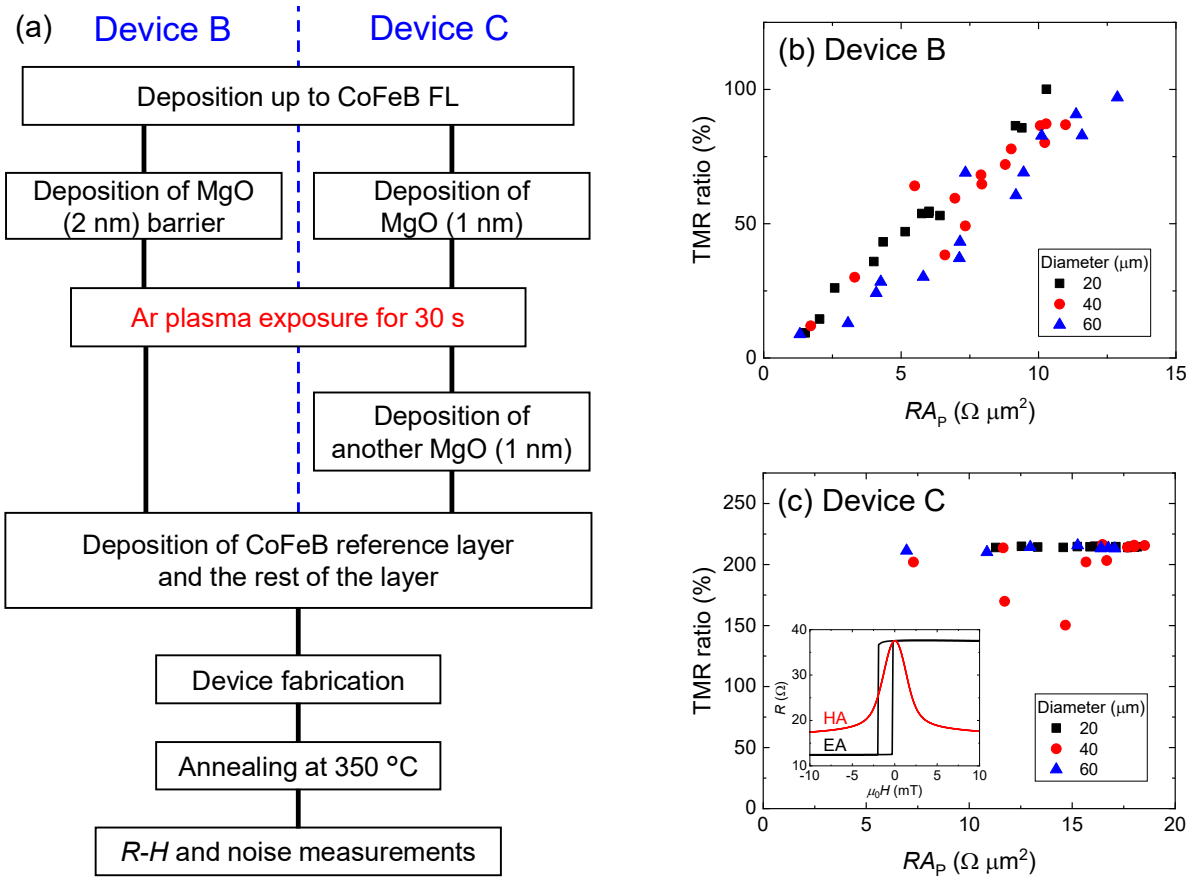

FIG. S1. (a) Flowchart of the Ar plasma exposure process to the MgO barrier. (b) and (c) Distribution of *RA* in the parallel magnetization state (RA_P) and TMR ratio of the individual devices with diameters of 20−60 μm of devices B and C, respectively.

Next, we compare the 1/*f* noise levels of the devices including device A. Figure S2(a) shows the noise spectra of these devices at $H_y = 0$, where the magnetizations of the soft-pinned FL and reference layer are in the antiparallel (AP) configuration. Sample B showed a very high 1/*f* noise level with a Hooge parameter of $\alpha_H = 4.6\times10^{-6}$ μm^2, due to the electrical 1/*f* noise caused by the lattice defects induced by the Ar plasma. On the other hand, sample C showed much lower 1/*f* noise with $\alpha_H = 1.6\times10^{-8}$ μm^2, comparable to that of sample A, $\alpha_H = 1.8\times10^{-8}$ μm^2. Figure 2(b) shows the H_y-dependence of α_H of devices A and C, both of which shows an increase in α_H with increasing H_y. Thus, the 1/*f* noise of device C is dominated by the magnetic 1/*f* noise as well as device A.

These results indicate that the Ar plasma damage induced in the lower half of the MgO barrier in sample C was healed by the deposition of another half of the MgO barrier, although the mechanism is not clear at present. Possibly, the lattice defects on the MgO surface caused by the Ar plasma, such as oxygen vacancies, are recovered by another MgO deposition. On the other hand, since device C showed a similar 1/*f* noise level as that of device A, the Ar plasma damage to the soft-pinned FL is considered to be negligible. Therefore, we believe that the Ar plasma exposure process to the MgO barrier induces lattice defects only on the MgO surface, which enhances the intensity of the electrical 1/*f* noise.

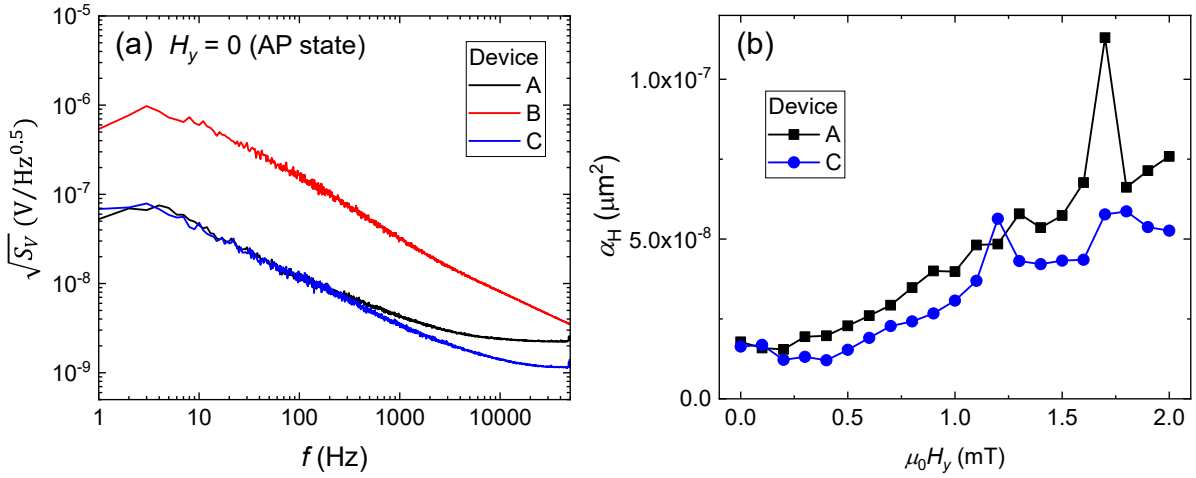

FIG. S2. (a) Noise spectra of devices A, B, and C at H_y = 0. The higher white noise level of device A than that of device C is due to the higher resistance of device A (R_{AP} = 182.5 Ω) than that of device C (R_{AP} = 37.6 Ω). (b) Dependence of the Hooge parameter (α_H) on the bias field H_y for devices A and C.